Coupling of fully symmetric As phonon to magnetism in Ba(Fe$_{1-x}$Au$_x$)$_2$As$_2$

S.-F. Wu,[1,*] W.-L. Zhang,[1,†] L. Li,[2] H.-B. Cao,[3] H.-H. Kung,[1] A. S. Sefat,[2] H. Ding,[4,5] P. Richard,[6] and G. Blumberg ●[1,7,‡]

[1]*Department of Physics and Astronomy, Rutgers University, Piscataway, New Jersey 08854, USA*
[2]*Materials Science & Technology Division, Oak Ridge National Laboratory, Oak Ridge, Tennessee 37831, USA*
[3]*Neutron Scattering Division, Oak Ridge National Laboratory, Oak Ridge, Tennessee 37831, USA*
[4]*Beijing National Laboratory for Condensed Matter Physics, and Institute of Physics, Chinese Academy of Sciences, Beijing 100190, China*
[5]*School of Physical Sciences, University of Chinese Academy of Sciences, Beijing 100190, China*
[6]*Institut quantique, Université de Sherbrooke, 2500 Boulevard de l'Université, Sherbrooke, Québec J1K 2R1, Canada*
[7]*National Institute of Chemical Physics and Biophysics, 12618 Tallinn, Estonia*

We study the coupling of the fully symmetric vibration mode of arsenic atoms to magnetism in a Ba(Fe$_{1-x}$Au$_x$)$_2$As$_2$ system by polarization-resolved Raman spectroscopy and neutron diffraction. In this system, there are two phase transitions: a tetragonal-to-orthorhombic structural phase transition at temperature T_S and a magnetic phase transition into collinear spin-density wave (SDW) state at temperature T_N ($\leqslant T_S$). T_S and T_N almost coincide in the pristine compound, whereas they differ by as much as 8 K for compounds with dilute gold substitution for iron. Raman coupling to the A_g(As) phonon is forbidden for the XY scattering geometry in the tetragonal phase above T_S, whereas it becomes allowed in the orthorhombic phase below T_S: The emerging mode's intensity indicates the lattice orthorhombicity. We find that upon cooling below T_S, first, weak A_g(As) phonon mode intensity appears in the XY scattering geometry spectra; however, the mode's intensity is significantly enhanced in the magnetic phase below T_N. The A_g(As) phonon also shows an asymmetric line shape below T_N and an anomalous linewidth broadening upon Au doping. We describe the anomalous behavior of the A_g(As) mode in the XY scattering geometry using a Fano model involving the A_g(As) phonon interacting with the $B_{2g}(D_{4h})$-symmetry-like electron-hole continuum. We conclude that the temperature dependence of light coupling amplitude to the A_g(As) phonon follows the evolution of the magnetic order parameter $M(T)$. We propose that the intensity enhancement of the A_g(As) phonon in the XY scattering geometry below T_N is due to electronic anisotropy induced by the collinear SDW order parameter.

I. INTRODUCTION

Our understanding of the superconducting and normal states in iron-based superconductors (FeSCs) remains insufficient due to their multiband and multiorbital nature, as well as complicated interplay among the spin, orbital, charge, and lattice degrees of freedom [1–7]. In particular, it has been noticed that the magnetic and electronic properties of FeSCs are sensitive to the buckling of the FeAs structure, namely, the As height with respect to the Fe-Fe plane, and to the related Fe-As-Fe bond angle of the Fe-As tetrahedra [8–19]. These parameters are modulated by the c-axis vibration of an As atom, corresponding to a fully symmetric phonon As mode (Fig. 1) [20–22]. Time-resolved x-ray diffraction experiments underline the importance of electron coupling to the As phonon with a fully symmetric deformation potential for the magnetic properties of the iron pnictides [23].

Raman spectroscopy is a suitable tool to *directly* probe the fully symmetric As phonon across the structural and magnetic phase transitions in iron pnictides. Various phonon anomalies for the fully symmetric As mode in the magnetic phase have been reported through Raman scattering measurements [24–29], signifying the coupling between the fully symmetric As phonon and magnetism in iron pnictides [30]. Among the phonon anomalies, a significant enhancement of the As phonon intensity measured in an unfavorable XY scattering geometry with cross-polarized light along the Fe-As directions [Fig. 1(a)] has been reported by a Raman study of a variety of parent compounds in FeSCs [29]. This intensity enhancement was found only for compounds with a magnetically ordered phase, such as BaFe$_2$As$_2$, LaFeAsO, and NaFeAs [25–27,29], in contrast to FeSe or LiFeAs compounds for which the phase of magnetic order is absent [28,29]. This enhancement was interpreted as originating from either electron-phonon coupling [30] or the resonance effect, owing to the high energy anisotropies [28]. In addition to the intensity enhancement, this fully symmetric As mode could show an asymmetric line shape in the XY scattering geometry below the magnetic phase transition temperature (T_N), as was reported for Ba(Fe$_{1-x}$Co$_x$)$_2$As$_2$ [25,26]. The asymmetric line shape signifies a Fano interference
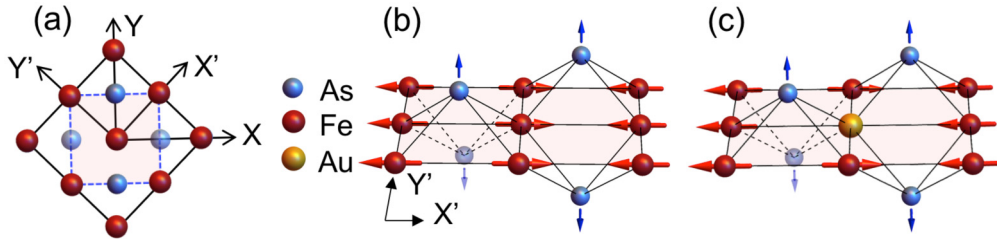
FIG. 1. Crystal structure of one As-Fe-As layer in $Ba(Fe_{1-x}Au_x)_2As_2$. (a) Definition of the X, Y, X', and Y' directions in tetragonal 2-Fe unit cell above T_S (red shaded area) and orthorhombic 4-Fe magnetic unit cell below T_N (black solid lines). (b) Schematic diagram of the magnetic ordering and of the fully symmetric As phonon mode. The red arrows mark Fe magnetic moments in the collinear antiferromagnetic phase. The blue arrows indicate the As c-axes displacement. (c) Illustration of local disorder by a nonmagnetic Au in the Fe plane of $Ba(Fe_{1-x}Au_x)_2As_2$.

pattern [31], whereas the line shape is affected by parameters such as the coupling strength, the density of the electronic continuum states, and the light coupling amplitude to the phonon and to the electronic continuum [32]. Unfortunately, the microscopic role of these parameters on the fully symmetric As mode coupling to magnetism below T_N and the relationship between these parameters and the magnetic order parameter still remain unclear.

In this paper, we close this knowledge gap by studying the coupling of the fully symmetric As mode to the magnetism in a $Ba(Fe_{1-x}Au_x)_2As_2$ system as a function of light Au doping and temperature through Raman scattering. In this system, T_S and T_N are determined by neutron diffraction and are found to differ by as much as 8 K. The fully symmetric As phonon shows an enhanced intensity and asymmetric line shape in the XY scattering geometry only at temperatures below T_N. The data can be consistently described by a Fano model involving the As phonon interacting with the XY symmetrylike electron-hole continuum. The fitting of the As phonon to the Fano model reveals that the light coupling amplitude to the As phonon in the XY scattering geometry (t_{ph}) is proportional to the magnetic order parameter $M(T)$ below T_N, indicating the collinear spin-density wave (SDW) order-induced electronic anisotropy is essential for the As phonon intensity enhancement. Interestingly, we also find an anomalous broadening of the As mode linewidth upon Au doping, which is limited only to the magnetic phase.

The rest of this paper is organized as follows. In Sec. II, we describe the sample preparations, neutron diffraction measurements, Raman scattering setup, and group theoretical analysis of the selection rules for the D_{4h} and D_{2h} point groups. In Sec. III, we present and discuss the experimental results. Specifically, in Sec. III A, we show the polarization dependence of the fully symmetric As phonon at $180 \, cm^{-1}$ in the XX, XY, $X'X'$ scattering geometries; In Sec. III B, we show the temperature dependence of the frequency and linewidth for Fe phonon at approximately $210 \, cm^{-1}$ in the $X'Y'$ scattering geometry; In Sec. III C, we present a Fano model fitting of the fully symmetric As phonon in the XY scattering geometry below T_N and discuss the fitting parameters. In Sec. III D, we present a phenomenological interpretation of the enhanced light coupling amplitude to the fully symmetric As mode in the XY scattering geometry (t_{ph}) in the magnetic phase. Finally, in Sec. IV, we provide a summary of our observations and conclusions.

II. EXPERIMENT AND METHODS

A. Crystal preparation

Single crystals of electron-doped $Ba(Fe_{1-x}Au_x)_2As_2$ ($x = 0, 0.012, 0.014,$ and 0.031) were grown out of self-flux using a high-temperature solution-growth technique described in Refs. [33,34] and the chemical compositions were determined by inductive coupled plasma analysis [34].

B. Neutron diffraction measurements

Neutron diffraction measurements on Au-doped samples were performed using the four-circle diffractometer HB-3A at the High Flux Isotope Reactor (HFIR) at the Oak Ridge National Laboratory to distinguish the structural and magnetic transitions. A neutron wavelength of 1.542 Å was used from a bent perfect Si-220 monochromator [35]. The corresponding structural phase transition temperatures (T_S) for $Ba(Fe_{1-x}Au_x)_2As_2$ are determined by the temperature evolution of the integrated intensity of lattice Bragg peak (2 2 0) in the tetragonal phase to (4 0 0) in the orthorhombic phase (Fig. 2). The corresponding magnetic phase transition temperatures (T_N) are determined for each sample composition from the temperature evolution of the magnetic Bragg peak intensities (1/2 1/2 5) in the tetragonal phase to (1 0 5) in the orthorhombic phase (Fig. 2). The T_S and T_N for the parent compound $BaFe_2As_2$ are determined by resistivity and magnetic susceptibility measurements [34,36]. All the T_S and T_N values for $Ba(Fe_{1-x}Au_x)_2As_2$ are summarized in Table I.

TABLE I. Summary of the structural and magnetic phase transition temperatures (Kelvin) for samples studied in this paper. The last column is the ordered moment (μ_B) per Fe at 4 K determined by neutron scattering measurements [36,37].

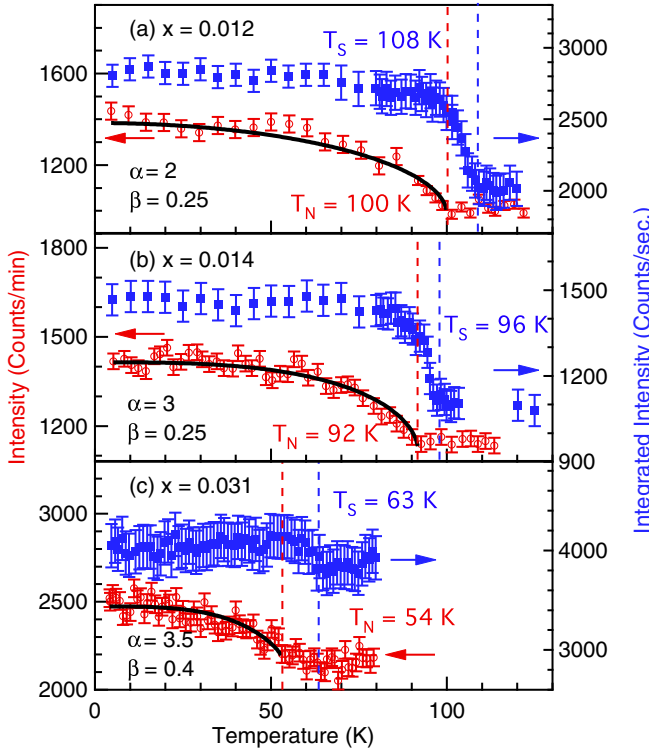| Sample	T_S	T_N	M
$BaFe_2As_2$	135	135	0.87 [5]
$Ba(Fe_{0.988}Au_{0.012})_2As_2$	108	100	0.50 ± 0.02
$Ba(Fe_{0.986}Au_{0.014})_2As_2$	96	92	0.42 ± 0.04
$Ba(Fe_{0.969}Au_{0.031})_2As_2$	63	54	0.36 ± 0.02

FIG. 2. Neutron diffraction results for $Ba(Fe_{1-x}Au_x)_2As_2$. (a) $x = 0.012$, (b) $x = 0.014$, and (c) $x = 0.031$. The blue solid squares represent temperature evolution of the integrated intensity of the lattice Bragg peak $(2\,2\,0)$ in the tetragonal phase, which develops into a $(4\,0\,0)$ Bragg peak in the orthorhombic phase. The red open circles represent temperature evolution of $(1\,0\,5)$ magnetic Bragg peak intensity in the orthorhombic phase. The blue and red dashed lines mark T_S and T_N, respectively. The black solid curves are the fits of the temperature evolution of the intensity of magnetic Bragg peak $(1\,0\,5)$ with the formula $I(T) = a[1 - (T/T_N)^\alpha]^{2\beta}$.

C. Raman scattering measurements

The crystals used for Raman scattering study were cleaved and positioned in a continuous helium flow optical cryostat. The Raman measurements were performed using the Kr^+ laser line at 647.1 nm (1.92 eV) in a quasibackscattering geometry along the crystallographic c axis. The excitation laser beam was focused into a 50×100 μm^2 spot on the ab surface, with the incident power around 10 mW. The scattered light was collected and analyzed by a triple-stage Raman spectrometer and recorded using a liquid nitrogen-cooled charge-coupled detector. The instrumental resolution was maintained better than 1.5 cm^{-1}. All linewidth data presented in this paper have been corrected for the instrumental resolution.

The laser heating in the Raman experiments was determined by imaging the appearance of stripe patterns due to twin domain formation at the structural phase transition temperature T_S [26]. When stripes appear under laser illumination, the spot temperature is just slightly below T_S, thus $T_S = kP + T_{cryo}$, where T_{cryo} is the temperature of cold helium gas in the cryostat, P is the laser power, and k is the heating coefficient. By recording T_{cryo} when the stripes appear at different laser powers, we have deduced the heating coefficient using a linear fit: $k = 1 \pm 0.1$ K/mW.

TABLE II. Summary of symmetry analysis in the D_{4h} and D_{2h} point groups [39].

Geometry	D_{4h}	D_{2h}
XX	$A_{1g} + B_{1g}$	$A_g + B_{1g}$
		not a proper geometry
XY	$A_{2g} + B_{2g}$	$A_g + B_{1g}$
		not a proper geometry
$X'X'$	$A_{1g} + B_{2g}$	A_g
$X'Y'$	$A_{2g} + B_{1g}$	B_{1g}
ZZ	A_{1g}	A_g

In this paper, we define the X and Y directions along the two-Fe unit cell basis vectors (at 45° from the Fe-Fe directions) in the tetragonal phase, whereas X' and Y' are along the Fe-Fe directions, see Fig. 1 [38]. The Z direction corresponds to the c axis perpendicular to the Fe-As plane. The Raman spectra have been recorded from the ab surface for $(\hat{e}_i\hat{e}_s) = (XX)$, (XY), $(X'X')$, and $(X'Y')$ polarization configurations, where $\hat{e}_i$ and $\hat{e}_s$ represent the incident and scattered light polarizations.

D. Group theoretical analysis

The body-centered crystal structure of $BaFe_2As_2$ above T_S belongs to the space group $I4/mmm$ (point group D_{4h}). Below T_S, the space group symmetry lowers to $Fmma$ (point group D_{2h}), and the magnetic phase transition does not change the lattice group symmetry.

For the D_{4h} point group, the Raman selection rules indicate that the XX, XY, $X'X'$, and $X'Y'$ polarization geometries probe the $A_{1g} + B_{1g}$, $A_{2g} + B_{2g}$, $A_{1g} + B_{2g}$, and $A_{2g} + B_{1g}$ symmetry excitations, respectively. In the orthorhombic phase with D_{2h} point-group symmetry, the unit cell rotates by 45°. The A_{1g} and B_{2g} representations of the D_{4h} point group merge into the A_g representation of the D_{2h} point group, and A_{2g} and B_{1g} (D_{4h}) merge into B_{1g} (D_{2h}). Notably, in the orthorhombic phase, the XX and XY polarization geometries are no longer proper, whereas the $X'X'$ and $X'Y'$ polarizations correspondingly probe the A_g and B_{1g} representations of the D_{2h} point group. Symmetry analysis for the point groups D_{4h} and D_{2h} are summarized in Table II.

In this paper, we focus on the nondegenerate Raman active phonon modes, namely, A_{1g}/A_g(As) phonon and B_{1g}(Fe) phonon, both of which are lattice vibrations along the c-axis direction. These two modes are accessible in a pseudobackscattering geometry from the ab surface. For XY scattering geometry, the A_{1g} mode is forbidden above T_S, but is allowed below T_S.

III. RESULTS AND DISCUSSIONS

A. A_{1g}/A_g(As) phonon at 180 cm^{-1}

In Figs. 3(a)–3(d), we show detailed temperature evolution of Raman response for $Ba(Fe_{1-x}Au_x)_2As_2$ ($x = 0$, 0.012, 0.014, and 0.031) in the XY scattering geometry. The T_S and T_N values, as determined by neutron diffraction data (Fig. 2), are indicated for each panel.
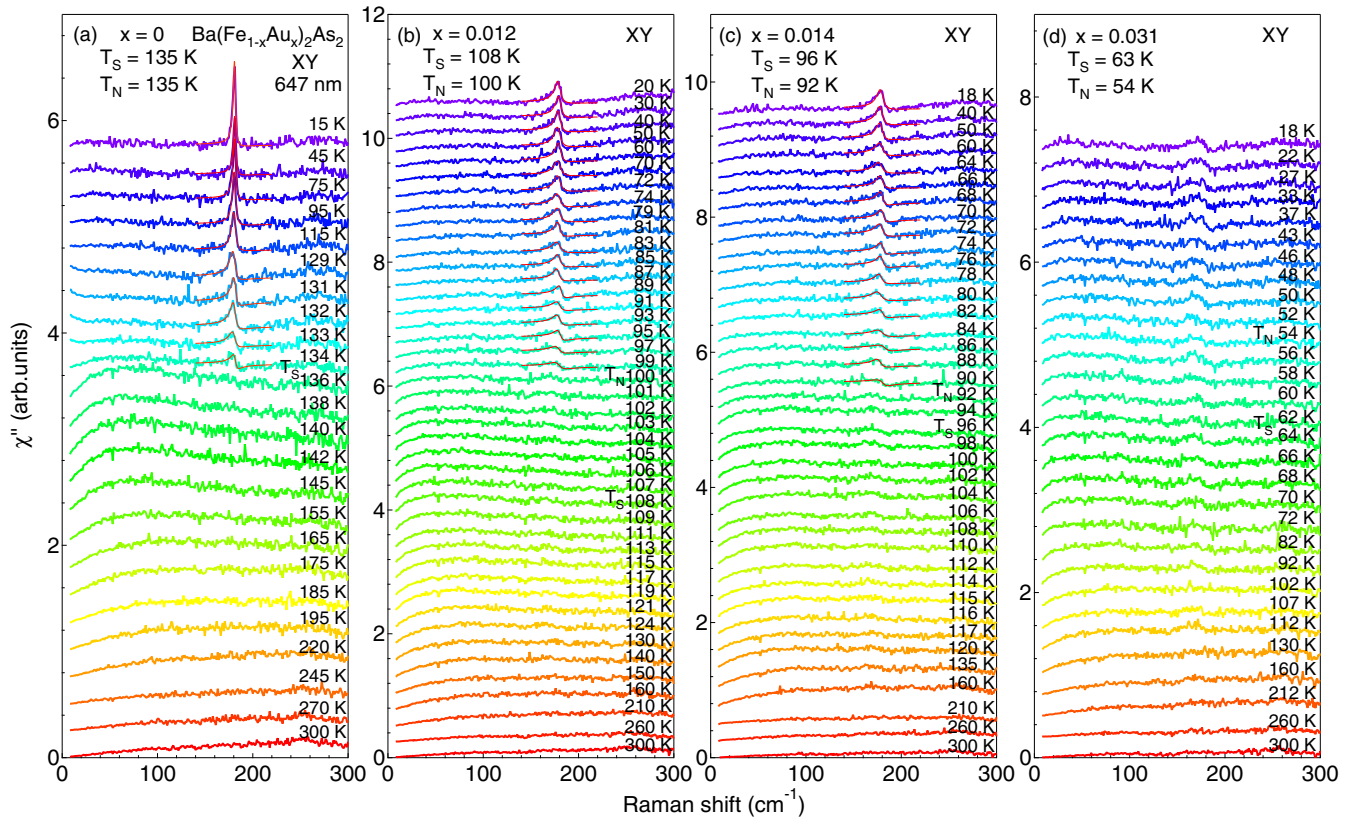
FIG. 3. T dependence of Raman spectra in the XY scattering geometry for $Ba(Fe_{1-x}Au_x)_2As_2$. (a) $x = 0$, (b) $x = 0.012$, (c) $x = 0.014$, (d) $x = 0.031$. The solid red line are fits for the $A_g(As)$ phonon mode using Eq. (3). The spectral resolution is $0.85\,cm^{-1}$.

For the parent compound $BaFe_2As_2$, see Fig. 3(a), the $A_g(As)$ phonon mode appears instantly below 134 K, which is close to $T_S (= T_N)$, with an asymmetric line shape. The phonon mode rapidly sharpens upon cooling and becomes more symmetric.

For $Ba(Fe_{0.988}Au_{0.012})_2As_2$, T_S and T_N are 108 K and 100 K, respectively. The temperature evolution of the $A_g(As)$ phonon spectra is displayed in Fig. 3(b). The very weak mode is difficult to detect between T_S and T_N (see Appendix E). The mode gains its strength only upon cooling below T_N, indicating that the magnetic phase is essential for the enhancement of the $A_g(As)$ phonon intensity. Although the asymmetry of the phonon line shape decreases upon cooling, it remains more asymmetric than for the pristine $BaFe_2As_2$ crystal. The behavior is similar to the Co-doped $BaFe_2As_2$ system [26].

We also report a similar observation for $Ba(Fe_{0.986}Au_{0.014})_2As_2$ and $Ba(Fe_{0.969}Au_{0.031})_2As_2$ crystals [Figs. 3(c) and 3(d)], although the line shape of the $A_g(As)$ mode broadens owing to disorder introduced by Au doping [40].

In Figs. 4(a) and 4(b), we compare the doping evolution of the $A_{1g}/A_g(As)$ phonon in the $X'X'$ scattering geometry at 300 K and 20 K. At 300 K, in the nonmagnetic phase, the $A_{1g}(As)$ phonon is symmetric and shows a nearly doping-independent mode frequency, linewidth and intensity. The symmetric Lorentzian line shapes are also clearly seen in the temperature dependence of the $A_{1g}(As)$ phonon above T_S (Fig. 5). In Fig. 4(b), we illustrate the contrasting behavior at 20 K for the $A_g(As)$ phonon in the magnetic phase: Here, upon

gold substitution for iron, we observe a significant linewidth broadening, intensity weakening, frequency softening, and a pronounced line-shape asymmetry. Similar behavior in the magnetic phase is also observed in the XY scattering geometry at 20 K [Fig. 4(c)]. In contrast, in the XX scattering geometry, the $A_g(As)$ phonon shows a symmetric line shape, see Fig. 6, although its intensity is much weaker than for the XY and
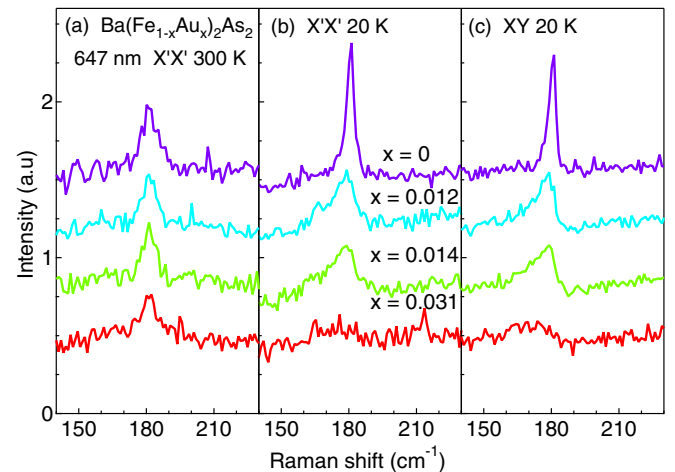

FIG. 4. The doping dependence of the $A_{1g}(As)$ phonon Raman intensity for $Ba(Fe_{1-x}Au_x)_2As_2$ (a) in the $X'X'$ scattering geometry at 300 K and (b) at 20 K. (c) Raman intensity in the XY scattering geometry at 20 K.

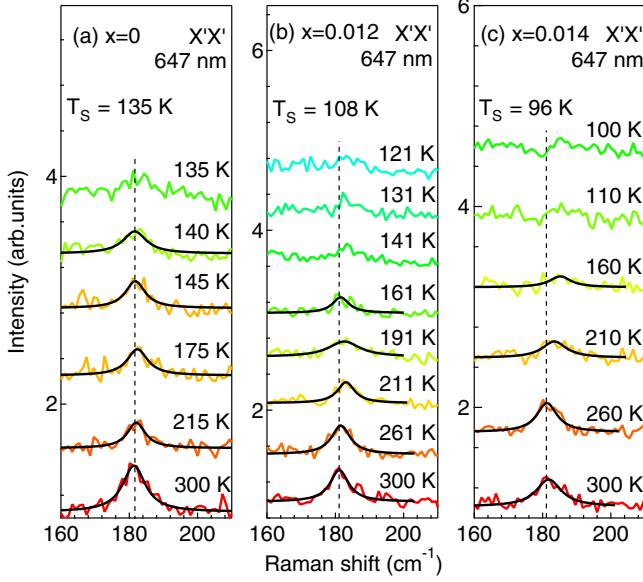FIG. 5. T dependence of the A_{1g}(As) phonon in the $X'X'$ scattering geometry above T_S for Ba(Fe$_{1-x}$Au$_x$)$_2$As$_2$. (a) $x = 0$, (b) $x = 0.012$, (c) x=0.014. The black solid lines are Lorentzian fits.

$X'X'$ scattering geometries. Similarly, in the ZZ scattering geometry [41], the A_{1g}/A_g(As) phonon mode remains symmetric across both the structural and magnetic phase transitions.

The asymmetric line shape of the A_g(As) phonon mode in the XY and $X'X'$ scattering geometries below T_N indicates a Fano interference pattern [31,32]. The appearance of such a Fano-shaped phonon requires both (1) an electronic continuum at the phonon energy in the same symmetry channel and (2) an interaction between the phonon and the electronic continuum.

To understand the symmetry-channel-dependent asymmetric line shape of the A_g(As) phonon, we utilize the polarization selection rules indicated in Table II. We see that both XY and $X'X'$ scattering geometries contain the $B_{2g}[D_{4h}]$-like
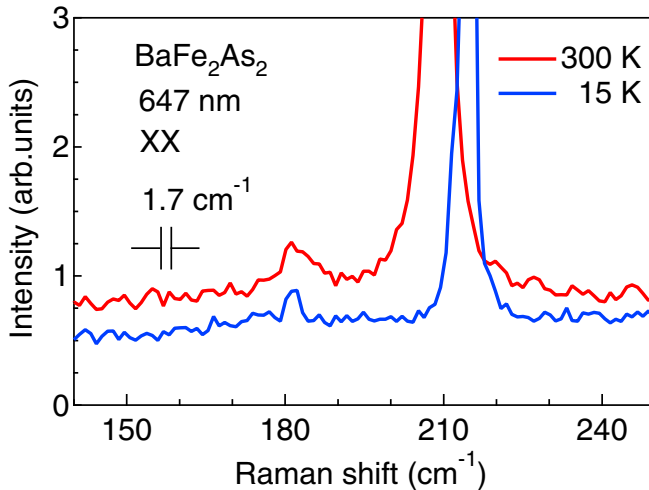

FIG. 6. Raman spectra in the XX scattering geometry at 300 K and 15 K for BaFe$_2$As$_2$.

excitation signals, whereas the XX, ZZ, and $X'Y'$ scattering geometries do not. As A_{1g} and B_{2g} representations merge into the A_g irreducible representation below the $D_{4h} \rightarrow D_{2h}$ transition, the $B_{2g}[D_{4h}]$-like electronic continuum is allowed to couple to the A_g(As) phonon in the XY and $X'X'$ scattering geometries below T_S, where asymmetric line shapes in these two scattering geometries occurs. Moreover, in the XY scattering geometry the A_g(As) phonon intensity is very weak within the temperature range between T_S and T_N where the magnetic ordering is absent, but the intensity becomes enhanced when magnetic ordering develops below T_N, see Fig. 3.

The polarization and temperature-dependent Raman spectra (Figs. 3–6) suggest that both the magnetic order and the electron-phonon coupling involving the A_g(As) mode and the $B_{2g}[D_{4h}]$-like electronic continuum are required for the two observations below T_N: the A_g(As) phonon intensity enhancement and the asymmetry line shapes in the XY and $X'X'$ scattering geometries.

B. B_{1g}(Fe) phonon at 210 cm^{-1}

Before moving forward with quantitative analysis of the asymmetric A_g(As) phonon line shape, it is instructive to take a closer look at the B_{1g} phonon, associated with the vibration of the Fe atom along the c axis. While below the tetragonal-to-orthorhombic transition, the A_g(As) phonon is symmetry allowed to couple to the $B_{2g}[D_{4h}]$-like electronic continuum, such coupling is not possible for the B_{1g}(Fe) phonon, and accordingly, the line shape of this mode in the $X'Y'$ geometry remains symmetric for all temperatures. However, *a priori* the B_{1g}(Fe) phonon could couple to the B_{1g}-like electronic continuum. To investigate this possibility, we display in Fig. 7 the temperature evolution of the B_{1g}(Fe) phonon at different Au-doping levels.

For the parent compound BaFe$_2$As$_2$, the B_{1g}(Fe) phonon frequency smoothly hardens upon cooling without detected anomalies around T_S/T_N. By contrast, the linewidth of the B_{1g}(Fe) mode decreases upon cooling and displays a discontinuity around T_S/T_N, see Figs. 7(a) and 8(a) [42].

For Au-doped Ba(Fe$_{1-x}$Au$_x$)$_2$As$_2$, the B_{1g}(Fe) phonon frequency shows similar behavior as for the parent compound, see Figs. 8(b)–8(d). The linewidth decreases upon cooling, however, the discontinuity around T_S/T_N is not apparent for the Au-doped alloys. This is likely due to disorder effects which smear out the structure and magnetic phase transitions.

The symmetric line shape of B_{1g}(Fe) phonon implies lack of coupling between the phonon and B_{1g}-symmetry electronic continuum.

We fit the temperature dependence of the phonon frequency and linewidth by an anharmonic phonon decay model [43,44]:

$$\omega_{B_{1g}}(T) = \omega_{0,B_{1g}} - C\left(1 + \frac{2}{e^{\frac{\hbar\omega_0}{2k_BT}} - 1}\right), \quad (1)$$

$$\gamma_{B_{1g}}(T) = \gamma_{0,B_{1g}} + \gamma'_{B_{1g}}\left(1 + \frac{2}{e^{\frac{\hbar\omega_0}{2k_BT}} - 1}\right). \quad (2)$$

The resulting fitting parameters are summarized in Table III. The B_{1g}(Fe) phonon frequency shows a very small softening upon Au doping. The elastic scattering $\gamma_{0,B_{1g}}$
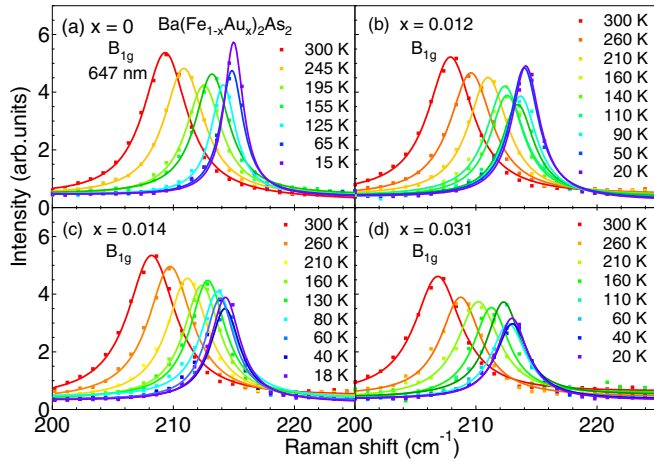
FIG. 7. T dependence of the B_{1g}(Fe) phonon in the $X'Y'$ geometry for Ba(Fe$_{1-x}$Au$_x$)$_2$As$_2$. (a) $x = 0$, (b) $x = 0.012$, (c) $x = 0.014$, (d) $x = 0.031$. The solid lines are the Lorentzian fits.

increases from nondetectably small for pristine crystal to only 0.7 cm^{-1} for the $x = 0.031$ alloy. The latter is in contrast to a significant linewidth broadening for the A_g(As) Fano-shaped feature, see Fig. 4.

C. Fano model and A_{1g}/A_g(As) phonon data analysis

In the following, we study interaction between the A_g(As) phonon and magnetism by investigating the A_g(As) phonon intensity and line shape in the XY scattering geometry below T_N. For this purpose, we introduce a Fano model in which the A_g(As) phonon couples to the $B_{2g}[D_{4h}]$-like electronic continuum (Fig. 9). The resulting line shape, which describes

TABLE III. Summary of fitting parameters for B_{1g}(Fe) phonon mode in Ba(Fe$_{1-x}$Au$_x$)$_2$As$_2$. All values are given in cm^{-1}.

Sample	$\omega_{0,B_{1g}}$	C	$\gamma_{0,B_{1g}}$	$\gamma'_{B_{1g}}$
BaFe$_2$As$_2$	217.3	2.0	small	0.3
Ba(Fe$_{0.988}$Au$_{0.012}$)$_2$As$_2$	216.5	2.0	0.5	0.4
Ba(Fe$_{0.986}$Au$_{0.014}$)$_2$As$_2$	216.3	2.0	0.5	0.4
Ba(Fe$_{0.969}$Au$_{0.031}$)$_2$As$_2$	215.1	1.9	0.7	0.4

the interference between a discrete phonon mode and an electronic continuum, has the following form [31,32,46], see also Appendix A:

$$\chi''(\omega) = t_e^2 \frac{\pi \rho (\omega_0 - \omega - v \frac{t_{ph}}{t_e})^2}{(\omega_0 - \omega)^2 + (v^2 \pi \rho)^2}, \qquad (3)$$

where v is the coupling constant between the phonon and the electronic continuum; t_{ph} and t_e are the light coupling amplitudes to the phonon and to the electronic continuum in the XY scattering geometry, respectively, (Fig. 9); ω_0 is the bare phonon frequency; and $\rho(\omega)$ is the density states of the electronic excitations. In the vicinity of the phonon frequency ω_0, for example, between 140 and 220 cm^{-1}, $\rho(\omega)$ can be considered frequency independent.

In Fig. 3, we employ the Fano model [see Eq. (3)] to fit the asymmetric mode line-shape data. For the best minimization result, we choose four independent parameter combinations $\{\frac{v}{t_e}, t_{ph}, \rho\pi t_e^2, \text{ and } \omega_0\}$ (see justification in Appendix B). Equations (B5) relate these combinations to the canonical Fano model parameters, see Eqs. (B2). The temperature dependence of the resulting parameter combinations $\{\frac{v}{t_e}, t_{ph},$
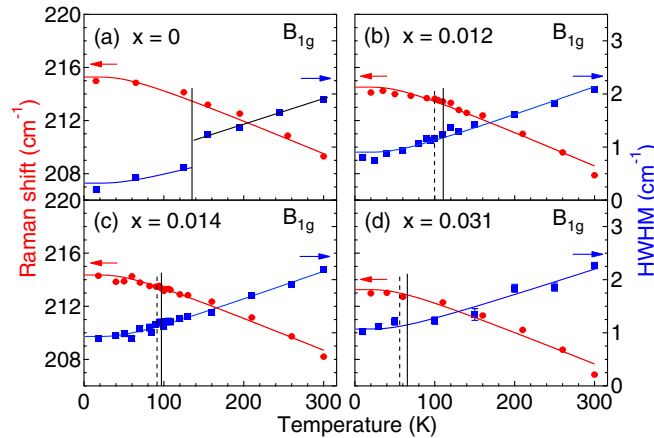

FIG. 8. Temperature dependence of the B_{1g}(Fe) phonon frequency $\omega_{B_{1g}}(T)$ (red dots) and the line shape half width at half maximum (HWHM) $\gamma_{B_{1g}}(T)$ (blue squares) for Ba(Fe$_{1-x}$Au$_x$)$_2$As$_2$. Data has been corrected for instrumental resolution. (a) $x = 0$, (b) $x = 0.012$, (c) $x = 0.014$, and (d) $x = 0.031$. The solid red lines are fits for the T dependence of the mode frequency using Eq. (1), whereas the solid blue lines are fits for the T dependence of the HWHM using Eq. (2). The vertical dashed lines represent T_N. The vertical solid black lines correspond to T_S, when it is different from T_N.

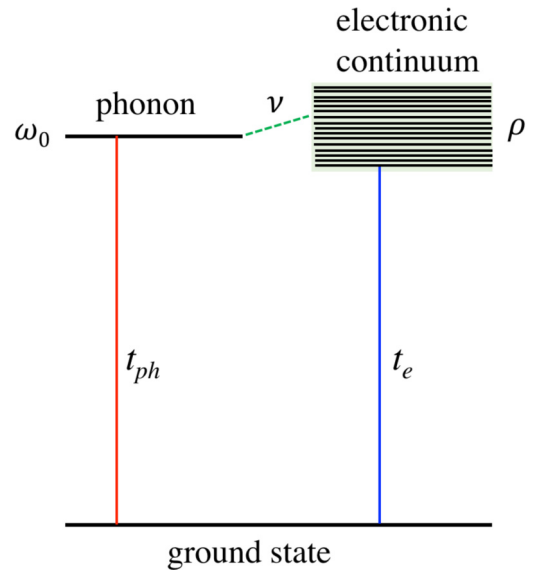FIG. 9. Schematic diagram of the energy levels involved in the electron-phonon coupling process [32]. t_{ph} and t_e are the light coupling amplitudes to the phonon and to the electronic continuum in the XY scattering geometry, respectively; ω_0 is the bare phonon frequency; $\rho(\omega)$ is the density states of the electronic excitations; v is the coupling constant between the phonon and the continuum.
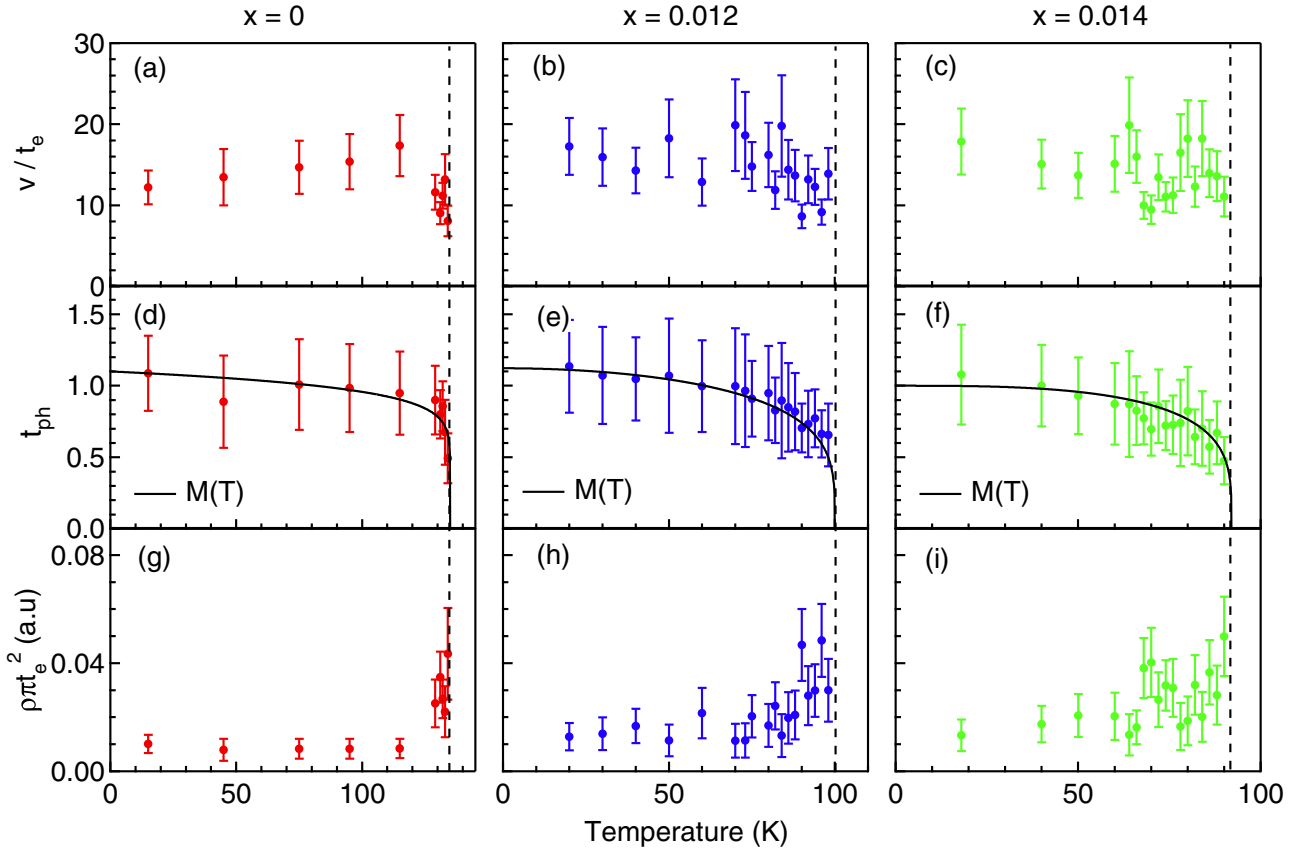
FIG. 10. Derived fitting parameters. (a)–(c) T dependence of electron-phonon coupling constant v/t_e, (d)–(f) the light coupling amplitude to the phonon t_{ph}, and (g)–(i) the intensity of the electronic continuum $\rho\pi t_e^2$. The dashed vertical lines are T_N for $Ba(Fe_{1-x}Au_x)_2As_2$. The solid black lines in (d)–(f) are the T dependence of the ordered magnetic moment $M(T)$. For $BaFe_2As_2$, $M(T) = a(1 - T/135)^{0.103}$ is obtained by fitting the temperature evolution of the $(1\,0\,3)$ magnetic Bragg peak intensity [45]. For Au-doped $Ba(Fe_{1-x}Au_x)_2As_2$ samples, $M(T) = b[1 - (T/T_N)^\alpha]^\beta$ is obtained by fitting the $(1\,0\,5)$ Bragg peak intensity below T_N using $I(T) = c[1 - (T/T_N)^\alpha]^{2\beta}$ (Fig. 2). In (d)–(f), $M(T)$ has been scaled to match the derived fitting parameters.

$\rho\pi t_e^2$} and the corresponding canonical parameters {A, q, Γ, ω_0, and the background intensity d } are shown in Figs. 10 and 12, respectively. Below we quantitatively discuss the doping and temperature dependence of the canonical Fano param-

eters, assuming that the light coupling vertex to electronic continuum t_e is independent on the doping and temperature.

The light coupling amplitude to phonon $t_{ph}(T)$ increases upon cooling below T_N, resembling the temperature
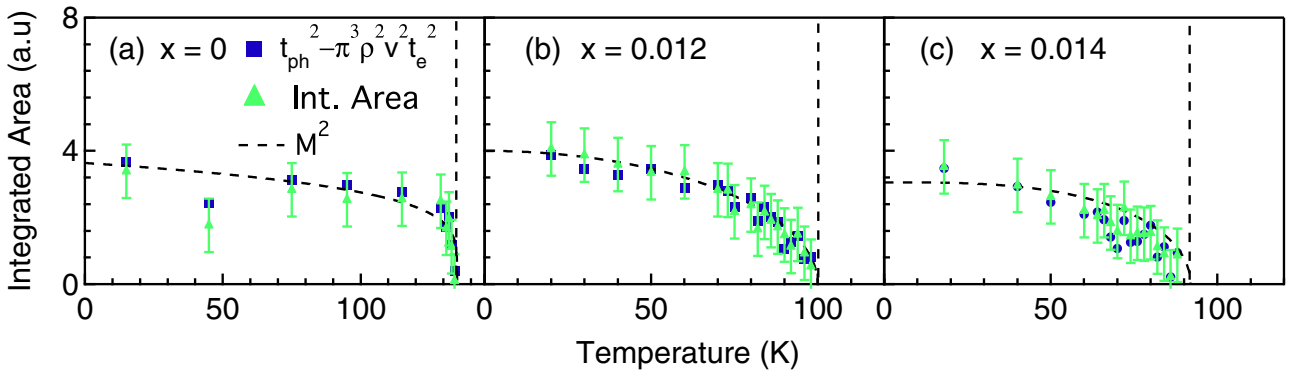
FIG. 11. T dependence of integrated area of the Fano-shaped phonon with respect to the electronic continuum for $Ba(Fe_{1-x}Au_x)_2As_2$: (a) $x = 0$, (b) $x = 0.012$, (c) $x = 0.014$. The dashed vertical lines represent the T_N values for each doping. The blue filled squares represent the integrated area calculated using the formula $\pi t_{ph}^2 - \pi^3 \rho^2 v^2 t_e^2$ [see Eq. (D4)]. The green filled triangles are calculated by integrating the spectra intensity between 140 and 220 cm^{-1} with respect to the fitted height of the electronic continuum $(d + A)$ [Fig. 14(f)]. The black dashed lines represent the scaled magnetic order parameter square $M(T)^2$.

FIG. 12. Temperature dependence of fitting parameters A (a)–(c), Γ (d)–(f), ω_0 (g)–(i), q (j)–(l), and d (m)–(o), using Eq. (B1) for Ba(Fe$_{1-x}$Au$_x$)$_2$As$_2$ ($x = 0$, 0.012, 0.014). The dashed vertical lines represent the T_N values for each doping concentration.
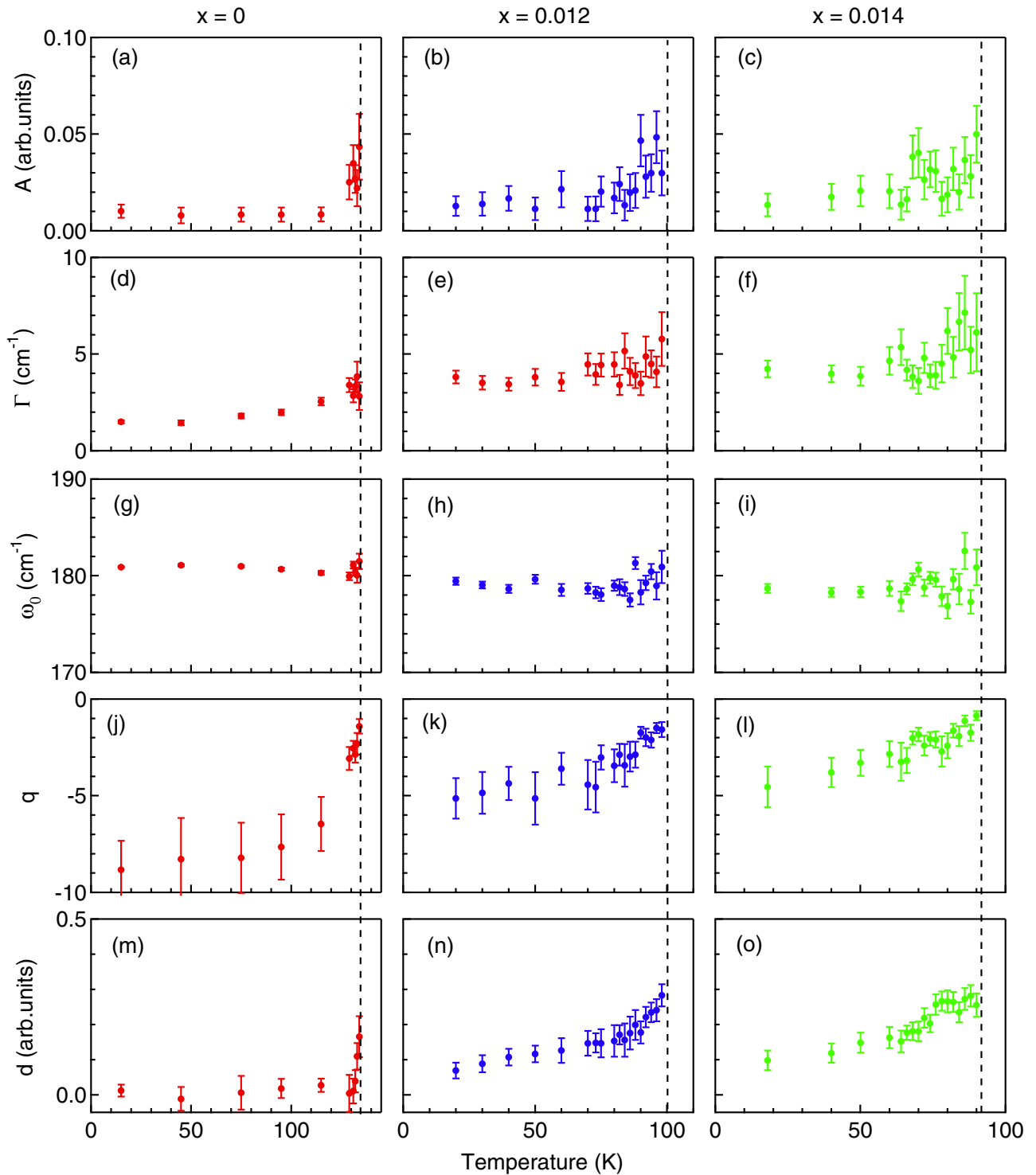
dependence of an order parameter, see Figs. 10(d)–10(f). In particular, we observe that $t_{ph}(T)$ is proportional to the magnetic order parameter $M(T)$ derived from the magnetic Bragg peak intensity (Fig. 2). To verify, we also integrate the spectral intensity above the continuum between 140 and 220 cm^{-1} that includes the A_g(As) phonon. As shown in

Fig. 11, the integrated area increases upon cooling below T_N. Interestingly, we find that it follows the square of the magnetic order parameter $M(T)^2$ (Fig. 11). Furthermore, the integrated area of the A_g(As) phonon with respect to the continuum can also be calculated from the fitting parameters $\pi t_{ph}^2 - \pi^3 \rho^2 v^2 t_e^2$ [Appendix D, see Eq. (D4)]. As we display

in Fig. 11, the two methods produce consistent results. In particular, when the A_g(As) phonon acquires a substantial intensity below T_N, the first term πt_{ph}^2 dominates the total integral, whereas the second term $-\pi^3 \rho^2 v^2 t_e^2$ contributes only a small correction (Appendix D). Thus, πt_{ph}^2 can be approximately scaled to $M(T)^2$, consistent with the fitting result $t_{ph} \sim M(T)$ [Figs. 10(d)–10(f)]. Therefore both the analysis of the integrated area of the A_g(As) phonon intensity [Fig. 11] and the direct fitting result of $t_{ph} \sim M(T)$ [Figs. 10(d)–10(f)] consistently demonstrate that the anomalous intensity increase of the A_g(As) phonon in SDW state is mainly due to the increase of the light coupling vertex.

The intensity of the electronic continuum represented by the parameter $\rho \pi t_e^2$ decreases upon cooling [47], which is consistent with the opening of a SDW gap [25,48–50]. This observation provides a natural explanation for asymmetry reduction of the Fano line shape upon cooling deep into SDW state [25].

The electron-phonon interaction strength parameter v/t_e appears below T_N and remains finite upon cooling [51]. The interaction weakly increases with Au doping, see Figs. 10(a)–10(c).

The Fano feature linewidth parameter $\Gamma = \pi \rho v^2$ increases threefold from $1.5\,\text{cm}^{-1}$ for pristine crystal to $4.5\,\text{cm}^{-1}$ for $x = 0.014$ alloy in the 20 K data, see Figs. 12(d)–12(f). This effect is consistent with independently derived 1.3 ± 0.7 times increase in the density of states ρ and 1.5 ± 0.4 times increase in the electron-phonon coupling v, see Fig. 10.

D. Enhancement of t_{ph} below T_N

After establishing that the A_g(As) phonon intensity enhancement in the XY scattering geometry below T_N is mainly due to $t_{ph} \sim M(T)$, we now focus on the physical meaning of parameter t_{ph}, as well as how the magnetic order affects the parameter t_{ph} below T_N.

On the phenomenological level, t_{ph} can be described as the Raman tensor element of the corresponding point group [52]. The $A_{1g}^{D_{4h}}$ and $A_g^{D_{2h}}$ Raman tensors have the following forms:

$$A_{1g}^{D_{4h}} = \begin{pmatrix} \bar{a} & 0 & 0 \\ 0 & \bar{a} & 0 \\ 0 & 0 & \bar{c} \end{pmatrix},$$

$$A_g^{D_{2h}} = \begin{pmatrix} \frac{(\bar{a}'+\bar{b}')}{2} & \frac{(\bar{a}'-\bar{b}')}{2} & 0 \\ \frac{(\bar{a}'-\bar{b}')}{2} & \frac{(\bar{a}'+\bar{b}')}{2} & 0 \\ 0 & 0 & \bar{c} \end{pmatrix},$$

where $A_g^{D_{2h}}$ (orthorhombic phase) has been rotated by $45°$ to maintain the same XYZ axis notation as in the tetragonal phase, and $\bar{a}'$ and $\bar{b}'$ are the diagonal elements of the $A_g^{D_{2h}}$ Raman tensor in the natural coordinate system of the orthorhombic phase [29]. For the A_{1g}(As) phonon in the XY scattering geometry, in the tetragonal phase, t_{ph} is zero. Below T_S, $\bar{a}'$ and $\bar{b}'$ are inequivalent, thus t_{ph} obtains a nonzero value of $t_{ph} \sim |\bar{a}' - \bar{b}'|/2$. In particular, in the nonmagnetic orthorhombic phase, because the A_g(As) phonon intensity is very weak (Fig. 3), t_{ph} is negligibly small. In the magnetic phase, because the A_g(As) phonon intensity is enhanced (Fig. 3), t_{ph} is large [53].

The enhancement of t_{ph} below T_N can be qualitatively understood as originating from the electronic anisotropy owing to the magnetic ordering in the magnetic phase. To begin, the electronic bands around E_F are sensitive to the As height relative to Fe-Fe plane as revealed by ultrafast photoemission measurements [20–22] and theoretical calculations [8,11,12,54,55], thus the bands around E_F are dynamically modulated by the A_g(As) phonon. Moreover, owing to the band folding along the X' direction as a result of the magnetic ordering below T_N, the band dispersions along the $k_{X'}$ and $k_{Y'}$ become strongly anisotropic ($k_{X'}$ direction is the folding direction and $k_{Y'}$ direction is orthogonal to $k_{X'}$ direction in k space) [56–62]. Consequently, the electronic bands along the $k_{X'}$ and $k_{Y'}$ directions have different effective mass, thus different rigidity to be modulated by the A_g(As) phonon. Thus, the enhancement of the A_g(As) mode in the XY geometry takes place only below T_N, instead of below T_S, because the anisotropy of electronic bands becomes prominent only below T_N [63].

We note that García-Martínez *et al.* [30] proposed that enhancement of the electron-phonon coupling v and of the Raman vertex t_{ph} both contribute to the intensity increase for the A_g(As) phonon in XY scattering geometry in the magnetic phase. The latter is related to the electronic anisotropy induced by collinear SDW phase.

IV. CONCLUSIONS

In summary, we employed polarization-resolved Raman spectroscopy to study a $\text{Ba(Fe}_{1-x}\text{Au}_x)_2\text{As}_2$ system in which the temperatures of structural (T_S) and magnetic (T_N) transitions split. We analyze evolution of the coupling between a fully symmetric phonon mode associated with the As ion c-axis vibration and magnetism as function of temperature and Au doping concentration x.

We demonstrate that intensity of the A_g(As) mode in XY scattering geometry just below T_S is very weak but it rapidly increases upon cooling below T_N. We also show that the A_g(As) mode's line shape in the magnetic phase is asymmetric and that asymmetry diminishes upon cooling deep into SDW state. To explain the evolution of intensity and line shapes below T_N, we adopt the Fano model, considering interaction between A_g(As) phonon and $B_{2g}(D_{4h})$-like electronic continuum. The Fano model fits to the Raman data reveal that coupling between phonon and continuum is only weakly enhanced in the magnetic phase. Instead, the light coupling amplitude to the phonon t_{ph} is strongly enhanced below T_N, following the temperature dependence of the magnetic order parameter $M(T)$. We propose that the electronic anisotropy induced by collinear-SDW-order is responsible for enhancement of t_{ph} below T_N. The effect of the mode's asymmetry reduction upon cooling is explained by monotonic suppression of the $B_{2g}(D_{4h})$-like continuum as the SDW gap opens when the magnetic order develops.

When nonmagnetic Au atom is substituted for magnetic Fe at a few percentage levels, the B_{1g}(Fe) phonon associated with the Fe c-axis vibration shows only a slight broadening, owing to enhanced elastic scattering. In contrast, the width of the Fano feature below T_N in XY scattering geometry shows threefold broadening with 1.4% Au doping which, besides the

impurity effects, we relate to a mild increase in the electron-phonon interaction strength with doping.

Finally, the phonon model analysis developed in this paper can be applied to a variety of systems to determine the underlying mechanism for phonon intensity and line-shape anomalies across different phases as a function of the external tuning parameters, such as the temperature, strain, pressure, and magnetic field.

APPENDIX A: DERIVATION OF EQ. (3)

In this Appendix, we derive the Fano model Eq. (3). We consider the interference between a discrete phonon mode and an interacting continuum [31,32,46]. The bare Raman response of discrete phonon mode is described by Lorentzian with frequency ω_0 and HWHM γ. The electronic continuum has the form of $-R(\omega) + i\rho(\omega)$, where its real and imaginary parts, $R(\omega)$ and $\rho(\omega)$, are connected by the Kramers-Kronig relations. Following Klein's approach [32,46], the Raman response of the perturbed system can be obtained as follows:

$$\chi''(\omega) = t_e^2 [\pi \rho(\omega)(\omega_0 - \omega - vt_{ph}/t_e)^2 + \gamma (vR(\omega)$$
$$- t_{ph}/t_e)^2 + \pi \rho(\omega)\gamma(v^2\pi\rho(\omega) + \gamma)]/$$
$$[(\omega_0 - \omega + v^2R(\omega))^2 + (v^2\pi\rho(\omega) + \gamma)^2] \quad \text{(A1)}$$

To estimate the bare (noninteracting) mode's linewidth γ, we use the phononic response of the A_g(As) mode in the XX scattering geometry. We fit the A_g(As) phonon in the XX scattering geometry at 15 K with a Voigt function where the instrumental broadening has been measured independently and fixed in the fitting procedures as $0.85 \, \text{cm}^{-1}$. The derived HWHM is approximately $0.4 \pm 0.3 \, \text{cm}^{-1}$, smaller than the instrumental broadening parameter $0.85 \, \text{cm}^{-1}$ (Fig. 6). Thus, the resolution limited γ at 15 K suggests that in the parent compound the As bare mode linewidth is very narrow.

For the Au-doped compounds, the substitution disorder in the Fe-Fe plane introduces an inhomogeneous linewidth broadening. One way to estimate the As mode's broadening resulting from Au doping is to investigate the A_{1g}(As) phonon in the $X'X'$ scattering above T_S where the electron-phonon coupling is absent [Figs. 4(a) and 5]. From Lorentzian fits

to A_{1g}(As) phonon at room temperature, we learn that the HWHM increases only by $0.2 \, \text{cm}^{-1}$, from $3.9 \pm 0.4 \, \text{cm}^{-1}$ to $4.1 \pm 0.4 \, \text{cm}^{-1}$, when the Au doping varies from $x = 0$ to $x = 0.031$ (Fig. 5). Thus, the impurity scattering and disorder-induced inhomogeneous linewidth broadening are nonessential relative to the Fano broadening effect $\Gamma = \pi\rho v^2$ (see Fig. 12). Hence, we will neglect γ in the further analyses.

In the limit of $\gamma \to 0$, Eq. (A1) can be simplified to

$$\chi''(\omega) = \frac{t_e^2 \pi \rho(\omega)(\omega_0 - \omega - vt_{ph}/t_e)^2}{(\omega_0 - \omega + v^2R(\omega))^2 + (v^2\pi\rho(\omega))^2}. \quad \text{(A2)}$$

Then, for the Raman spectra, the mode is located at $\Omega = \omega_0 + v^2R(\omega)$, where $v^2R(\omega)$ represents the phonon energy shift owing to the renormalization by the electron-phonon coupling. We can estimate $v^2R(\omega)$ in $BaFe_2As_2$ based on the Raman spectra [Fig. 3(a) and 3(b)] in Ref. [29]. We find that the phonon energy shift between the bare mode (XX scattering geometry) and coupled mode (XY scattering geometry) is about $1 \, \text{cm}^{-1}$. Thus, we estimate that $v^2R(\omega)$ for $BaFe_2As_2$ at 15 K is about $1 \, \text{cm}^{-1}$, which is about 0.5% compared to the bare-mode frequency at $180 \, \text{cm}^{-1}$. Because we mainly focus on the Fano line shape originating from the imaginary part of the interacting continuum, rather than the phonon energy shift originating from the real part of the interacting continuum, we treat the renormalized mode's frequency as an effective ω_0 [64,65]. Thus, Eq. (A2) can be simplified to Eq. (3):

$$\chi''(\omega) = \frac{t_e^2 \pi \rho(\omega_0 - \omega - vt_{ph}/t_e)^2}{(\omega_0 - \omega)^2 + (v^2\pi\rho)^2}. \quad \text{(A3)}$$

APPENDIX B: FITTING MODEL

The fitting model in Eq. (3) can be rewritten into a form equivalent to the form originally given by Fano [31]:

$$\chi''(\omega) = A\frac{(\epsilon + q)^2}{1 + \epsilon^2}, \quad \text{(B1)}$$

where

$$\varepsilon = \frac{\omega - \omega_0}{\Gamma}, \, A = \pi\rho t_e^2, \, \Gamma = \pi\rho v^2, \, q = \frac{t_{ph}/t_e}{\rho\pi v}. \quad \text{(B2)}$$

As shown in Fig. 13, parameter A represents the intensity of the interacting continuum. When ω is far away from ω_0, $\chi''(\omega)$ asymptotically approaches to A. Parameter Γ is the HWHM of the coupled Fano-shaped mode. As we have assumed that the linewidth of the bare phonon is negligible (Appendix A), Γ mainly originates from the electron-phonon interaction. Dimensionless parameter q is inversely proportional to the electron-phonon interaction strength v. The evolution of the Fano line shape as a function of q is discussed below in Appendix C.

In the following, we demonstrate that parameters (A, Γ, q, ω_0) in Eq. (B1) can be uniquely determined by the Fano interference pattern. By solving the equation $\partial\chi''(\omega)/\partial\omega = 0$, we obtain the maximum and minimum peak positions. If $q < 0$, the peak minimum is located at $\omega_0 - q\Gamma$ and the minimum intensity is zero. This point is called Fano antiresonance (Fig. 13), and occurs when $\frac{\omega-\omega_0}{\Gamma} = -q$, because there is an exact cancellation between the phonon and continuum amplitudes at this energy. The peak maximum is located
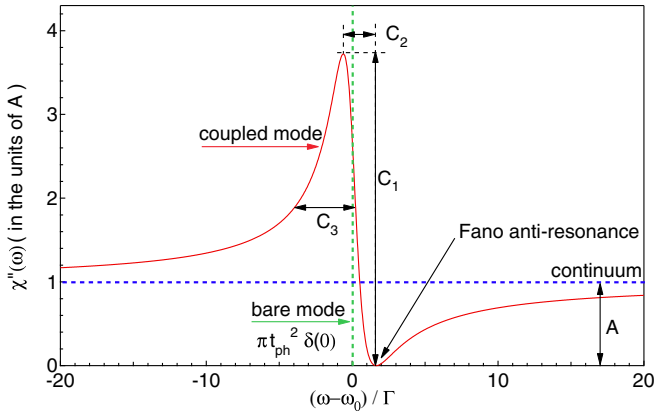
FIG. 13. An illustration of Fano-shaped mode. The blue dashed horizontal line represents the intensity of the interacting continuum A. The green vertical dashed line represents the bare mode $\pi t_{ph}^2 \delta(0)$. The maximum peak intensity with respect to the minimum intensity is illustrated as C_1. The distance in the frequency axis between the maximum and minimum peaks is illustrated as C_2. The FWHM is illustrated as C_3.

at $\omega_0 + \frac{\Gamma}{q}$ and the maximum intensity is $A(1 + q^2)$. The frequency difference between the maximum and minimum peaks is $|\Gamma(q + \frac{1}{q})|$. To obtain the full width at half maximum (FWHM) of the Fano line shape, we solve the equation $A\frac{(\epsilon + q)^2}{(1 + \epsilon^2)} = A(1 + q^2)/2$ and obtain two solutions: $\omega_1 = \omega_0 - \frac{\Gamma(q-1)}{q+1}$ and $\omega_2 = \omega_0 + \frac{\Gamma(q+1)}{q-1}$, thus the FWHM of the Fano-shaped mode is $|\omega_2 - \omega_1| = \frac{2\Gamma(q^2+1)}{|q^2-1|}$.

Given a Fano-shaped mode spectrum ($q < -1$), as an example illustrated in Fig. 13, we choose three measurable physical quantities, namely, the maximum peak intensity C_1, the energy difference between the maximum and minimum peaks C_2, and the FWHM C_3. By solving the following equations:

$$A(1 + q^2) = C_1,$$

$$-\Gamma\left(q + \frac{1}{q}\right) = C_2,$$

$$\frac{2\Gamma(q^2 + 1)}{q^2 - 1} = C_3,$$

(B3)

we obtain (A, Γ, q)

$$A = \frac{C_1 C_2^2 - C_1\sqrt{C_2^2 + C_3^2}C_2 + C_1 C_3^2}{2(C_2^2 + C_3^2)},$$

$$q = -\frac{C_2 + \sqrt{C_2^2 + C_3^2}}{C_3},$$

$$\Gamma = \frac{C_2 C_3}{2\sqrt{C_2^2 + C_3^2}}.$$

(B4)

Using Eqs. (B4), the parameters (A, Γ, q) can be uniquely determined from three measurable quantities (C_1, C_2, C_3). Taking the bare-mode frequency ω_0 into consideration, we conclude that four independent parameters (A, Γ, q, ω_0) in

Eq. (B1) can be uniquely determined by a Fano interference pattern, and vice versa.

We now turn to the relation between the fitting models given by Eqs. (3) and (B1). There are five parameters $(t_{ph}, t_e, \rho, v, \omega_0)$ in Eq. (3), whereas there are four parameters (A, Γ, q, ω_0) in Eq. (B1). Because ω_0 has the same definition in both fitting equations, four parameters (t_{ph}, t_e, ρ, v) remain in Eq. (3). Since parameters (A, Γ, q) in Eq. (B1) are independent, not all of the four parameters (t_{ph}, t_e, ρ, v) are independent. Because t_e is the light-electronic continuum vertex, its temperature and doping dependence are assumed to be weak. Therefore, we choose $(t_{ph}, \frac{v}{t_e}, \rho\pi t_e^2)$ as the three independent parameters in Eq. (3). Here, parameters $(t_{ph}, \frac{v}{t_e}, \rho\pi t_e^2)$ can be obtained via (A, Γ, q) using Eqs. (B2):

$$t_{ph} = |q|\sqrt{\Gamma A},$$

$$\frac{v}{t_e} = \sqrt{\frac{\Gamma}{A}},$$

$$\rho\pi t_e^2 = A.$$

(B5)

After the fitting parameters (A, Γ, q, ω_0) in Eq. (B1) are obtained by fitting to the Raman spectra in Fig. 3, the parameters $(t_{ph}, \frac{v}{t_e}, \rho\pi t_e^2, \omega_0)$ in Eq. (3) can be derived via Eqs. (B5).

The error bar of the parameters $(t_{ph}, \frac{v}{t_e}, \rho\pi t_e^2)$ can be also estimated from Eqs. (B5). For example, if $F = F(A, \Gamma, q)$, the error-bar δ_F is

$$\delta_F = \sqrt{\left(\frac{\partial F}{\partial A}\delta_A\right)^2 + \left(\frac{\partial F}{\partial \Gamma}\delta_\Gamma\right)^2 + \left(\frac{\partial F}{\partial q}\delta_q\right)^2}, \quad (B6)$$

where $(\delta_A, \delta_\Gamma, \delta_q)$ are the standard errors for the parameters (A, Γ, q).

Finally, we discuss the nonzero Fano antiresonance point for $Ba(Fe_{1-x}Au_x)_2As_2$ spectra. At the Fano antiresonance frequency, the Raman intensity is always zero according to Eq. (B1). However, such zero intensity at the Fano antiresonance frequency is not always observed in the data, e.g., Fig. 14(f). The nonzero minimum intensity might be partially owing to an imperfect background subtraction. To obtain the B_{2g} Raman response, the B_{1g} Raman background was subtracted from the raw intensity data of the B_{2g} response. The estimation of the B_{1g} background and the subtraction process might partially create this issue. Another possibility is that the A_g(As) phonon is superimposed on a noninteracting background [65–68], because there exists signals from the quasielastic scattering (Fig. 3), as well as the SDW scattering [25,48,50] at around the A_g(As) phonon energy below T_N. To account for the nonzero Fano antiresonance, we fit the Raman spectra using Eq. (B1) with a constant background parameter d. Therefore, the intensity of the electronic continuum parameter A (or $\rho\pi t_e^2$) we derived from the fitting is an effective one. An example of the relative values of parameters A and d is shown in Fig. 14(f). All fitting results, shown in Fig. 3, are in good agreement with the data.
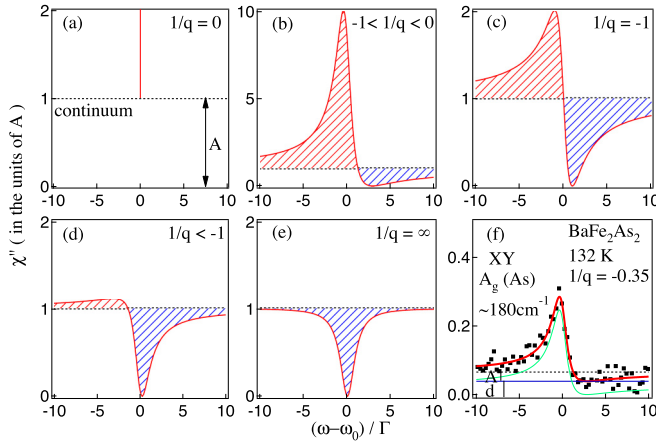
FIG. 14. Evolution of Fano line shape as a function of interaction strength $1/q$. (a) Noninteracting case where $1/q \rightarrow 0$. (b) Weakly interacting case where $-1 < 1/q < 0$, the integrated area of the Fano-shaped phonon with respect to the continuum is positive. (c) Strongly asymmetric case where $1/q = -1$, the integrated area of Fano-shaped phonon with respect to the continuum is zero because of the cancellation of positive and negative spectral regions. (d) Interacting case where $1/q < -1$, the integrated area of Fano-shaped phonon with respect to the continuum is negative. (e) Strongly interacting case where $1/q \rightarrow \infty$, the bare mode becomes a negative phonon peak with respect to the continuum. (f) Example of the Fano-shaped A_g(As) phonon for $BaFe_2As_2$ at 132 K in the XY scattering geometry. The solid red line is the fit by Eq. (B1) with a constant background d. The fitted $1/q$ is about -0.35. The green and blue solid lines are the Fano component [Eq. (B1)] and the background component (d), respectively. The dashed black line represents the intensity of the continuum (A) with respect to the intensity of the background d.

APPENDIX C: EVOLUTION OF THE FANO LINE SHAPE AS A FUNCTION OF q

In the following, we discuss the evolution of the Fano line shape [Eq. (B1)] as a function of q ($q < 0$) for various characteristic regimes.

(1) The noninteracting case is in the limit of $q \rightarrow -\infty$ ($1/q \rightarrow 0$). In this case, the bare phonon mode is infinitely sharp. From Eq. (A1), the limit of $v \rightarrow 0$ (equivalent of $q \rightarrow -\infty$), is trivial,

$$\rho \pi t_e^2 + \pi t_{ph}^2 \frac{\gamma/\pi}{(\omega - \omega_0)^2 + \gamma^2}, \tag{C1}$$

where $\frac{\gamma/\pi}{(\omega-\omega_0)^2+\gamma^2}$ is the normalized Lorentzian function. In the limit of $\gamma \rightarrow 0$, Eq. (C1) is

$$\rho \pi t_e^2 + \pi t_{ph}^2 \delta(\omega - \omega_0). \tag{C2}$$

As shown in Fig. 14(a), the bare phonon mode with spectra weight πt_{ph}^2 is superimposed over the electronic continuum $\rho \pi t_e^2$.

(2) In the regime where $q < -1$ ($-1 < 1/q < 0$), as shown in Fig. 14(b), interaction between the phonon and the continuum is weak. The destructive and constructive interferences affect the line shape of the phonon. The spectra weight is suppressed on the high-frequency side of the phonon and enhanced on the low-frequency side. Therefore, the

Dirac-δ-function-like discrete phonon starts to broaden and develops an asymmetric line shape. Although a negative intensity appears with respect to the continuum, the positive intensity with respect to the continuum dominates the entire integrated intensity of the phonon with respect to the continuum.

(3) When $q = -1$ ($1/q = -1$), as shown in Fig. 14(c), a highly asymmetric case occurs in which the positive and negative integrated intensities of the coupled mode with respect to the continuum exactly cancel, thus the total integrated intensity of phonon with respect to the continuum vanish.

(4) Within the regime of $-1 < q < 0$ ($1/q < -1$), as shown in Fig. 14(d), the positive intensity with respect to the continuum becomes weaker and the negative intensity with respect to the continuum becomes dominant. Thus, the entire integrated phonon intensity with respect to the continuum is negative.

(5) The limit of $q \rightarrow 0$ ($1/q \rightarrow -\infty$) corresponds to strongly interacting case. If an electron-phonon interaction occurs, with a finite t_e, ρ, and v, from Eq. (B2) we obtain $t_{ph} = q t_e \rho \pi v \rightarrow 0$. As shown in Fig. 14(e), the coupled mode appears as a dip with respect to the continuum [69]. Such an interference-induced dip is an inverse Lorentzian underneath the electronic continuum with vanishing intensity at $\omega = \omega_0$.

Note that when $q > 0$, the evolution of the Fano line shape as a function of q is similar as discussed above, except that the maximum and minimum peak positions of the coupled mode interchange.

APPENDIX D: INTEGRATED AREA OF THE FANO-SHAPED PHONON

In this Appendix, we discuss the integrated area of the Fano-shaped phonon with respect to continuum intensity. This can be obtained by integrating the Fano function $\chi''(\omega) = A(\epsilon + q)^2/(1 + \epsilon^2)$ [Eq. (B1)] shifted down by A within a limited spectra range $2B$ centered at ω_0, namely, $\int_{\omega_0-B}^{\omega_0+B}(\chi''(\omega) - A)d\omega$. The integration results in

$$2A\left(q^2 - 1\right)\Gamma \arctan\left(\frac{B}{\Gamma}\right). \tag{D1}$$

If $B \rightarrow \infty$, we obtain the limit:

$$A\Gamma\pi(q^2 - 1). \tag{D2}$$

We further simplify Eq. (D2) into Eq. (D3) using $t_{ph}^2 = q^2 \Gamma A$ [Eqs. (B5)]:

$$\pi t_{ph}^2 - A\Gamma\pi \tag{D3}$$

Using $A = \rho \pi t_e^2$ and $\Gamma = \rho \pi v^2$ [Eq. (B2)], we obtain equivalent forms of Eqs. (D2) and (D3):

$$\pi t_{ph}^2 - \pi^3 \rho^2 v^2 t_e^2. \tag{D4}$$

In particular, from Eq. (D2), when $|q| \gg 1$, the first term $A\Gamma\pi q^2$ (πt_{ph}^2) dominates the integrated area of the Fano-shaped mode with respect to the continuum, because the second term $A\Gamma\pi$ ($\pi^3 \rho^2 v^2 t_e^2$) contributes only to a small correction. For example, when $|q| = 10, 5, 3$, or 2, the correction is approximately 1%, 4%, 11%, or 25%, respectively. Note that when $|q|$ is close to 1, the
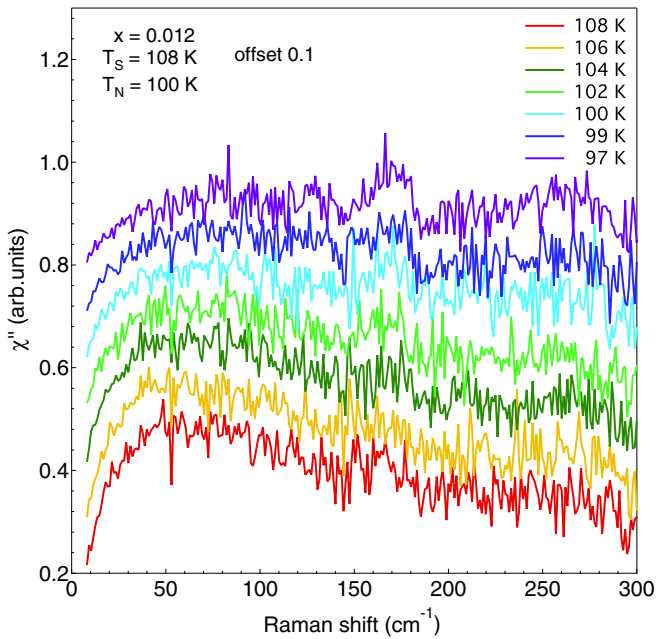
FIG. 15. Enlargement of the data from Fig. 3(b): Evolution of Raman response including the A_g(As) phonon as a function of temperature between T_S and T_N for the $x = 0.012$ sample.

integrated area with respect to the continuum tends to be zero.

For Ba(Fe$_{1-x}$Au$_x$)$_2$As$_2$, the temperature dependencies of fitting parameter q are shown in Figs. 12(j)–12(l). In general, $|q|$ varies from 1 to 9. For BaFe$_2$As$_2$ and Ba(Fe$_{0.988}$Au$_{0.012}$)$_2$As$_2$, when the A_g(As) phonon acquires a substantial intensity in the XY scattering geometry below T_N, most of the $|q|$ values are larger than 3, thus $A\Gamma\pi q^2$ (πt_{ph}^2) contributes more than 90% of the entire integrated area of the A_g(As) phonon below T_N. For Ba(Fe$_{0.986}$Au$_{0.014}$)$_2$As$_2$, half of the $|q|$ values are larger than 3, and most of the $|q|$ values are larger than 2, when $T < T_N - 10$ K. Therefore, $A\Gamma\pi q^2$ (πt_{ph}^2) contributes more than 75% of the entire integrated area of the A_g(As) phonon within the temperature range of $T < T_N - 10$ K.

Therefore, based on the fitting results in Figs. 12(j)–12(l), when the A_g(As) phonon acquires a substantial intensity in the XY scattering geometry below T_N, the first term πt_{ph}^2 dominates the entire integrated area of the A_g(As) phonon with respect to the continuum intensity.

APPENDIX E: A_g(As) PHONON BETWEEN T_S AND T_N

In Fig. 15, we focus on the spectra between $T_S = 108$ K and $T_N = 100$ K of the $x = 0.012$ alloy in Fig. 3(b). The A_g(As) phonon intensity is rather weak between T_S and T_N, whereas it is evident below T_N.

[1] J. Paglione and R. L. Greene, High-temperature superconductivity in iron-based materials, Nat. Phys. **6**, 645 (2010).

[2] F. Wang and D.-H. Lee, The electron-pairing mechanism of iron-based superconductors, Science **332**, 200 (2011).

[3] R. M. Fernandes and A. V. Chubukov, Low-energy microscopic models for iron-based superconductors: A review, Rep. Prog. Phys. **80**, 014503 (2016).

[4] P. J. Hirschfeld, Using gap symmetry and structure to reveal the pairing mechanism in Fe-based superconductors, C. R. Phys. **17**, 197 (2016).

[5] P. C. Dai, Antiferromagnetic order and spin dynamics in iron-based superconductors, Rev. Mod. Phys. **87**, 855 (2015).

[6] Q. M. Si, R. Yu, and E. Abrahams, High-temperature superconductivity in iron pnictides and chalcogenides, Nat. Rev. Mater. **1**, 16017 (2016).

[7] R. M. Fernandes, A. V. Chubukov, and J. Schmalian, What drives nematic order in iron-based superconductors? Nat. Phys. **10**, 97 (2014).

[8] K. Kuroki, H. Usui, S. Onari, R. Arita, and H. Aoki, Pnictogen height as a possible switch between high-T_c nodeless and low-T_c nodal pairings in the iron-based superconductors, Phys. Rev. B **79**, 224511 (2009).

[9] J. D. Lee, W. S. Yun, and S. C. Hong, Ultrafast above-transition-temperature resurrection of spin density wave driven by coherent phonon generation in BaFe$_2$As$_2$, New J. Phys. **16**, 043010 (2014).

[10] V. Balédent, F. Rullier-Albenque, D. Colson, J. M. Ablett, and J.-P. Rueff, Electronic Properties of BaFe$_2$As$_2$ Upon Doping and Pressure: The Prominent Role of the As p Orbitals, Phys. Rev. Lett. **114**, 177001 (2015).

[11] V. Vildosola, L. Pourovskii, R. Arita, S. Biermann, and A. Georges, Bandwidth and Fermi surface of iron oxypnictides: Covalency and sensitivity to structural changes, Phys. Rev. B **78**, 064518 (2008).

[12] M. J. Calderón, B. Valenzuela, and E. Bascones, Tight-binding model for iron pnictides, Phys. Rev. B **80**, 094531 (2009).

[13] Z. P. Yin, S. Lebègue, M. J. Han, B. P. Neal, S. Y. Savrasov, and W. E. Pickett, Electron-Hole Symmetry and Magnetic Coupling in Antiferromagnetic LaFeAsO, Phys. Rev. Lett. **101**, 047001 (2008).

[14] F. Yndurain, Coupling of magnetic moments with phonons and electron-phonon interaction in LaFeAsO$_{1-x}$F$_x$, EPL **94**, 37001 (2011).

[15] C. de la Cruz, W. Z. Hu, S. L Li, Q. Huang, J. W. Lynn, M. A. Green, G. F. Chen, N. L. Wang, H. A. Mook, Q. M Si, and P. C Dai, Lattice Distortion and Magnetic Quantum Phase Transition in CeFeAs$_{1-x}$P$_x$O, Phys. Rev. Lett. **104**, 017204 (2010).

[16] C. L. Zhang, L. W. Harriger, Z. P. Yin, W. C. Lv, M. Y. Wang, G. T. Tan, Y. Song, D. L. Abernathy, W. Tian, T. Egami, K. Haule, G. Kotliar, and P. C. Dai, Effect of Pnictogen Height on Spin Waves in Iron Pnictides, Phys. Rev. Lett. **112**, 217202 (2014).

[17] C. H Lee, A. Iyo, H. Eisaki, H. Kito, M. T. Fernandez-Diaz, T. Ito, K. Kihou, H. Matsuhata, M. Braden, and K. Yamada, Effect of structural parameters on superconductivity in

fluorine-free LnFeAsO$_{1-y}$ (Ln = La, Nd), J. Phys. Soc. Jpn. **77**, 083704 (2008).

[18] J. Zhao, Q. Huang, C. de la Cruz, S. L. Li, J. W. Lynn, Y. Chen, M. A. Green, G. F. Chen, G. Li, Z. Li, J. L. Luo, N. L. Wang, and P. C. Dai, Structural and magnetic phase diagram of CeFeAsO$_{1-x}$F$_x$ and its relation to high-temperature superconductivity, Nat. Mater. **7**, 953 (2008).

[19] G. Garbarino, R. Weht, A. Sow, C. Lacroix, A. Sulpice, M. Mezouar, X. Zhu, F. Han, H. H. Wen, and M. Núñez-Regueiro, Direct observation of the influence of the FeAs$_4$ tetrahedron on superconductivity and antiferromagnetic correlations in Sr$_2$VO$_3$FeAs, EPL **96**, 57002 (2011).

[20] I. Avigo, R. Cortés, L. Rettig, S. Thirupathaiah, H. S. Jeevan, P. Gegenwart, T. Wolf, M. Ligges, M. Wolf, J. Fink, and U. Bovensiepen, Coherent excitations and electron-phonon coupling in Ba/EuFe$_2$As$_2$ compounds investigated by femtosecond time- and angle-resolved photoemission spectroscopy, J. Phys.: Condens. Matter **25**, 094003 (2013).

[21] L. X. Yang, G. Rohde, T. Rohwer, A. Stange, K. Hanff, C. Sohrt, L. Rettig, R. Cortés, F. Chen, D. L. Feng, T. Wolf, B. Kamble, I. Eremin, T. Popmintchev, M. M. Murnane, H. C. Kapteyn, L. Kipp, J. Fink, M. Bauer, U. Bovensiepen, and K. Rossnagel, Ultrafast Modulation of the Chemical Potential in BaFe$_2$As$_2$ by Coherent Phonons, Phys. Rev. Lett. **112**, 207001 (2014).

[22] S. Gerber, S.-L. Yang, D. Zhu, H. Soifer, J. A. Sobota, S. Rebec, J. J. Lee, T. Jia, B. Moritz, C. Jia, A. Gauthier, Y. Li, D. Leuenberger, Y. Zhang, L. Chaix, W. Li, H. Jang, J.-S. Lee, M. Yi, G. L. Dakovski, S. Song, J. M. Glownia, S. Nelson, K. W. Kim, Y.-D. Chuang, Z. Hussain, R. G. Moore, T. P. Devereaux, W.-S. Lee, P. S. Kirchmann, and Z.-X. Shen, Femtosecond electron-phonon lock-in by photoemission and x-ray free-electron laser, Science **357**, 71 (2017).

[23] L. Rettig, S. O. Mariager, A. Ferrer, S. Grübel, J. A. Johnson, J. Rittmann, T. Wolf, S. L. Johnson, G. Ingold, P. Beaud, and U. Staub, Ultrafast Structural Dynamics of the Fe-Pnictide Parent Compound BaFe$_2$As$_2$, Phys. Rev. Lett. **114**, 067402 (2015).

[24] K.-Y. Choi, D. Wulferding, P. Lemmens, N. Ni, S. L. Bud'ko, and P. C. Canfield, Lattice and electronic anomalies of CaFe$_2$As$_2$ studied by Raman spectroscopy, Phys. Rev. B **78**, 212503 (2008).

[25] L. Chauvière, Y. Gallais, M. Cazayous, M. A. Méasson, A. Sacuto, D. Colson, and A. Forget, Raman scattering study of spin-density-wave order and electron-phonon coupling in Ba(Fe$_{1-x}$Co$_x$)$_2$As$_2$, Phys. Rev. B **84**, 104508 (2011).

[26] F. Kretzschmar, T. Bohm, U. Karahasanovic, B. Muschler, A. Baum, D. Jost, J. Schmalian, S. Caprara, M. Grilli, C. Di Castro, J. G. Analytis, J.-H. Chu, I. R. Fisher, and R. Hackl, Critical spin fluctuations and the origin of nematic order in Ba(Fe$_{1-x}$Co$_x$)$_2$As$_2$, Nat. Phys. **12**, 560 (2016).

[27] U. F. Kaneko, P. F. Gomes, A. F. García-Flores, J.-Q. Yan, T. A. Lograsso, G. E. Barberis, D. Vaknin, and E. Granado, Nematic fluctuations and phase transitions in LaFeAsO: A Raman scattering study, Phys. Rev. B **96**, 014506 (2017).

[28] A. Baum, Y. Li, M. Tomić, N. Lazarević, D. Jost, F. Löffler, B. Muschler, T. Böhm, J.-H. Chu, I. R. Fisher, R. Valentí, I. I. Mazin, and R. Hackl, Interplay of lattice, electronic, and spin degrees of freedom in detwinned BaFe$_2$As$_2$: A Raman scattering study, Phys. Rev. B **98**, 075113 (2018).

[29] S.-F. Wu, W.-L. Zhang, V. K.Thorsmølle, G. F. Chen, A. S. Sefat, Y. G. Shi, H. Ding, P. Richard, and G. Blumberg, Magneto-elastic coupling in Fe-based superconductors, arXiv:1712.01896.

[30] N. A. García-Martínez, B. Valenzuela, S. Ciuchi, E. Cappelluti, M. J. Calderón, and E. Bascones, Coupling of the As A_{1g} phonon to magnetism in iron pnictides, Phys. Rev. B **88**, 165106 (2013).

[31] U. Fano, Effects of configuration interaction on intensities and phase shifts, Phys. Rev. **124**, 1866 (1961).

[32] M. V. Klein, Electronic Raman scattering, in *Light scattering in Solids I*, Vol. 8, edited by M. Cardona (Springer-Verlag, Berlin, 1983), Chap. 4, pp. 147–202.

[33] A. S. Sefat, Bulk synthesis of iron-based superconductors, Curr. Opin. Solid State Mater. Sci. **17**, 59 (2013).

[34] L. Li, H. B. Cao, M. A. McGuire, J. S. Kim, G. R. Stewart, and A. S. Sefat, Role of magnetism in superconductivity of BaFe$_2$As$_2$: Study of 5d Au-doped crystals, Phys. Rev. B **92**, 094504 (2015).

[35] B. C. Chakoumakos, H. B. Cao, F. Ye, A. D. Stoica, M. Popovici, M. Sundaram, W. D. Zhou, J. S. Hicks, G. W. Lynn, and R. A. Riedel, Four-circle single-crystal neutron diffractometer at the high flux isotope reactor, J. Appl. Cryst. **44**, 655 (2011).

[36] L. Li, D. S. Parker, Z. Gai, H. B. Cao, and A. S. Sefat, Superconductivity with $T_c \approx 7$ K under pressure for Cu- and Au-doped BaFe$_2$As$_2$, J. Phys. Condens. Matter **32**, 295602 (2020).

[37] S.-F. Wu, W.-L. Zhang, L. Li, H. B. Cao, H.-H. Kung, A. S. Sefat, H. Ding, P. Richard, and G. Blumberg, On the origin of critical nematic fluctuations in Fe-based superconductors, arXiv:1712.06066.

[38] We note that in the orthorhombic phase, the *X* and *Y* directions are no longer at 45° to the Fe-Fe bonds. Consequently, below T_S the scattering geometries involving *X* and *Y* directions are referred to by us as improper.

[39] M. Cardona, Resonance phenomena, in *Light Scattering in Solids II*, Vol. 50, edited by M. Cardona and G. Güntherodt (Springer-Verlag, Berlin, 1982), Chap. 2, pp. 45–173.

[40] We note that for Ba(Fe$_{0.969}$Au$_{0.031}$)$_2$As$_2$ the selection rules are relaxed: A weak phonon intensity appears already above T_S [see Fig. 3(d)].

[41] X. Ren, L. Duan, Y. W. Hu, J. R. Li, R. Zhang, H. Q. Luo, P. C. Dai, and Y. Li, Nematic Crossover in BaFe$_2$As$_2$ Under Uniaxial Stress, Phys. Rev. Lett. **115**, 197002 (2015).

[42] L. Chauvière, Y. Gallais, M. Cazayous, A. Sacuto, M. A. Méasson, D. Colson, and A. Forget, Doping dependence of the lattice dynamics in Ba(Fe$_{1-x}$Co$_x$)$_2$As$_2$ studied by Raman spectroscopy, Phys. Rev. B **80**, 094504 (2009).

[43] P. G. Klemens, Anharmonic decay of optical phonons, Phys. Rev. **148**, 845 (1966).

[44] J. Menéndez and M. Cardona, Temperature dependence of the first-order Raman scattering by phonons in Si, Ge, and α-Sn: Anharmonic effects, Phys. Rev. B **29**, 2051 (1984).

[45] S. D. Wilson, Z. Yamani, C. R. Rotundu, B. Freelon, E. Bourret-Courchesne, and R. J. Birgeneau, Neutron diffraction study of the magnetic and structural phase transitions in BaFe$_2$As$_2$, Phys. Rev. B **79**, 184519 (2009).

[46] G. Blumberg, M. V. Klein, L. Börjesson, R. Liang, and W. N. Hardy, Investigation of the temperature dependence of

electron and phonon Raman scattering in single crystal YBa$_2$Cu$_3$O$_{6.952}$, J. Supercond. **7**, 445 (1994).

[47] We note that the background parameter d in Fig. 12(m)–12(o) also shows a temperature dependence. Parameter d accounts for the nonzero Fano antiresonance (see a discussion in Appendix B). In this sense, the intensity of the electronic continuum $\rho \pi t_e^2$ we derived herein is an effective one.

[48] W. Z. Hu, J. Dong, G. Li, Z. Li, P. Zheng, G. F. Chen, J. L. Luo, and N. L. Wang, Origin of the Spin Density Wave Instability in AFe$_2$As$_2$ (A=Ba,Sr) as Revealed by Optical Spectroscopy, Phys. Rev. Lett. **101**, 257005 (2008).

[49] P. Richard, K. Nakayama, T. Sato, M. Neupane, Y.-M. Xu, J. H. Bowen, G. F. Chen, J. L. Luo, N. L. Wang, X. Dai, Z. Fang, H. Ding, and T. Takahashi, Observation of Dirac Cone Electronic Dispersion in BaFe$_2$As$_2$, Phys. Rev. Lett. **104**, 137001 (2010).

[50] W.-L. Zhang, Z. P. Yin, A. Ignatov, Z. Bukowski, J. Karpinski, A. S. Sefat, H. Ding, P. Richard, and G. Blumberg, Raman scattering study of spin-density-wave-induced anisotropic electronic properties in AFe$_2$As$_2$ (A=Ca, Eu), Phys. Rev. B **93**, 205106 (2016).

[51] Parameter v refers to the coupling constant between the A_g(As) phonon and the B_{2g}(D_{4h})-like electronic continuum. The v value is finite only below T_S when A_{1g} and B_{2g} representations merge into the A_g irreducible representation below the $D_{4h} \rightarrow D_{2h}$ transition (Sec. III A and Table II).

[52] M. Chandrasekhar, J. B. Renucci, and M. Cardona, Effects of interband excitations on Raman phonons in heavily doped n-Si, Phys. Rev. B **17**, 1623 (1978).

[53] In the magnetic phase, $\bar{a}'$ and $\bar{b}'$ may have opposite signs [25] or nonzero imaginary parts [28].

[54] M. Zbiri, H. Schober, M. R. Johnson, S. Rols, R. Mittal, Y. X. Su, M. Rotter, and D. Johrendt, Ab initio lattice dynamics simulations and inelastic neutron scattering spectra for studying phonons in BaFe$_2$As$_2$: Effect of structural phase transition, structural relaxation, and magnetic ordering, Phys. Rev. B **79**, 064511 (2009).

[55] S. Gerber, K. W. Kim, Y. Zhang, D. Zhu, N. Plonka, M. Yi, G. L. Dakovski, D. Leuenberger, P. S. Kirchmann, R. G. Moore, M. Chollet, J. M. Glownia, Y. Feng, J.-S. Lee, A. Mehta, A. F. Kemper, T. Wolf, Y.-D. Chuang, Z. Hussain, C.-C. Kao, B. Moritz, Z.-X. Shen, T. P. Devereaux, and W.-S. Lee, Direct characterization of photoinduced lattice dynamics in BaFe$_2$As$_2$, Nat. Commun. **6**, 7377 (2015).

[56] M. Yi, D. Lu, J.-H. Chu, J. G. Analytis, A. P. Sorini, A. F. Kemper, B. Moritz, S.-K. Mo, R. G. Moore, M. Hashimoto, W.-S. Lee, Z. Hussain, T. P. Devereaux, I. R. Fisher, and Z.-X. Shen, Symmetry-breaking orbital anisotropy observed for detwinned Ba(Fe$_{1-x}$Co$_x$)$_2$As$_2$ above the spin density wave transition, Proc. Natl. Acad. Sci. USA **108**, 6878 (2011).

[57] M. D. Watson, P. Dudin, L. C. Rhodes, D. V. Evtushinsky, H. Iwasawa, S. Aswartham, S. Wurmehl, B. Büchner, M. Hoesch, and T. K. Kim, Probing the reconstructed Fermi surface

of antiferromagnetic BaFe$_2$As$_2$ in one domain, npj Quantum Mater. **4**, 36 (2019).

[58] H. Pfau, S. D. Chen, M. Yi, M. Hashimoto, C. R. Rotundu, J. C. Palmstrom, T. Chen, P.-C. Dai, J. Straquadine, A. Hristov, R. J. Birgeneau, I. R. Fisher, D. Lu, and Z.-X. Shen, Momentum Dependence of the Nematic Order Parameter in Iron-Based Superconductors, Phys. Rev. Lett. **123**, 066402 (2019).

[59] H. Pfau, C. R. Rotundu, J. C. Palmstrom, S. D. Chen, M. Hashimoto, D. Lu, A. F. Kemper, I. R. Fisher, and Z.-X. Shen, Detailed band structure of twinned and detwinned BaFe$_2$As$_2$ studied with angle-resolved photoemission spectroscopy, Phys. Rev. B **99**, 035118 (2019).

[60] M. Nakajima, T. Liang, S. Ishida, Y. Tomioka, K. Kihou, C. H. Lee, A. Iyo, H. Eisaki, T. Kakeshita, T. Ito, and S. Uchida, Unprecedented anisotropic metallic state in undoped iron arsenide BaFe$_2$As$_2$ revealed by optical spectroscopy, Proc. Natl. Acad. Sci. USA **108**, 12238 (2011).

[61] C. Mirri, A. Dusza, S. Bastelberger, M. Chinotti, L. Degiorgi, J.-H. Chu, H.-H. Kuo, and I. R. Fisher, Origin of the Resistive Anisotropy in the Electronic Nematic Phase of BaFe$_2$As$_2$ Revealed by Optical Spectroscopy, Phys. Rev. Lett. **115**, 107001 (2015).

[62] Z. P. Yin, K. Haule, and G. Kotliar, Magnetism and charge dynamics in iron pnictides, Nat. Phys. **7**, 294 (2011).

[63] We note that orbital ordering, which lifts the degeneracy of the d_{xz}/d_{yz} orbital below T_S, also contributes to the in-plane electronic anisotropy; however, this effect is weak compared with the magnetism in terms of reconstructing the electronic band structure [57].

[64] H.-H. Kung, M. Salehi, I. Boulares, A. F. Kemper, N. Koirala, M. Brahlek, P. Lošťák, C. Uher, R. Merlin, X. Wang, S.-W. Cheong, S. Oh, and G. Blumberg, Surface vibrational modes of the topological insulator Bi$_2$Se$_3$ observed by Raman spectroscopy, Phys. Rev. B **95**, 245406 (2017).

[65] A. Bock, S. Ostertun, R. Das Sharma, M. Rübhausen, K.-O. Subke, and C. T. Rieck, Anomalous self-energy effects of the B_{1g} phonon in Y$_{1-x}$(Pr,Ca)$_x$Ba$_2$Cu$_3$O$_7$ films, Phys. Rev. B **60**, 3532 (1999).

[66] G. Abstreiter, M. Cardona, and A. Pinczuk, Light scattering by free carrier excitations in semiconductors, in *Light Scattering in Solids IV*, Vol. 54, edited by M. Cardona and G. Güntherodt (Springer-Verlag, Berlin, 1984), Chap. 2, p. 127.

[67] V. G. Hadjiev, Xingjiang Zhou, T. Strohm, M. Cardona, Q. M. Lin, and C. W. Chu, Strong superconductivity-induced phonon self-energy effects in HgBa$_2$Ca$_3$Cu$_4$O$_{10+\delta}$, Phys. Rev. B **58**, 1043 (1998).

[68] S. Ostertun, J. Kiltz, A. Bock, U. Merkt, and T. Wolf, Superconductivity-induced changes of the phonon resonances in RBa$_2$Cu$_3$O$_7$ (R = Yb, Er, Sm, Nd), Phys. Rev. B **64**, 064521 (2001).

[69] E. Cappelluti, L. Benfatto, M. Manzardo, and A. B. Kuzmenko, Charged-phonon theory and Fano effect in the optical spectroscopy of bilayer graphene, Phys. Rev. B **86**, 115439 (2012).